

Learning OFDM Waveforms with PAPR and ACLR Constraints

Mathieu Goutay, *Student Member, IEEE*, Fayçal Ait Aoudia, *Member, IEEE*,
Jakob Hoydis, *Senior Member, IEEE*, and Jean-Marie Gorce,
Senior Member, IEEE

Abstract

An attractive research direction for future communication systems is the design of new waveforms that can both support high throughputs and present advantageous signal characteristics. Although most modern systems use orthogonal frequency-division multiplexing (OFDM) for its efficient equalization, this waveform suffers from multiple limitations such as a high adjacent channel leakage ratio (ACLR) and high peak-to-average power ratio (PAPR). In this paper, we propose a learning-based method to design OFDM-based waveforms that satisfy selected constraints while maximizing an achievable information rate. To that aim, we model the transmitter and the receiver as convolutional neural networks (CNNs) that respectively implement a high-dimensional modulation scheme and perform the detection of the transmitted bits. This leads to an optimization problem that is solved using the augmented Lagrangian method. Evaluation results show that the end-to-end system is able to satisfy target PAPR and ACLR constraints and allows significant throughput gains compared to a tone reservation (TR) baseline. An additional advantage is that no dedicated pilots are needed.

Index Terms

Deep learning, end-to-end learning, neural networks, OFDM, waveform, ACLR, PAPR

Mathieu Goutay is with Nokia Bell Labs, Paris-Saclay, 91620 Nozay, France, and also with the CITI Lab, INSA Lyon, Inria, Université de Lyon, 69100 Villeurbanne, France (e-mail: mathieu.goutay@nokia.com).

Fayçal Ait Aoudia and Jakob Hoydis were with Nokia Bell Labs, Paris-Saclay, 91620 Nozay, France. They are now with NVIDIA, 06906 Sophia Antipolis, France (e-mail: {faitaoudia, jhoydis}@nvidia.com).

Jean-Marie Gorce is with the CITI Lab, INSA Lyon, Inria, Université de Lyon, 69100 Villeurbanne, France (e-mail: jean-marie.gorce@insa-lyon.fr).

I. INTRODUCTION

The next generation of cellular networks will need to support a growing number of different services and devices [1]. Along with higher throughputs, future communication systems are expected to satisfy new requirements on the signal characteristics. For example, a higher number of connected devices suggests that the available spectrum should be more efficiently shared among users, challenging the need for guard bands. Moreover, the power amplifier (PA) nonlinearities in sub-THz systems lead to the use of large power backoffs to prevent distortions caused by high-amplitude signals. A key research direction to address these issues is the design of new waveforms. Among possible candidates, orthogonal frequency-division multiplexing (OFDM) is already used in most modern communication systems, including 4G, 5G, and Wi-Fi. The main benefits of OFDM are a very efficient hardware implementation and a single-tap equalization at the receiver. However, conventional OFDM suffers from multiple drawbacks, including the addition of pilots for channel equalization, a high sensitivity to Doppler spread, and both a high peak-to-average power ratio (PAPR) and adjacent channel leakage ratio (ACLR), which might hinder its use in beyond-5G systems.

Future base stations and user equipments are expected to be equipped with dedicated machine learning (ML) accelerators [2] that enable efficient implementation of neural network (NN)-based components. In this paper, we take advantage of such capabilities and propose a new learning-based approach to OFDM-based waveform design. This approach is based on a convolutional neural network (CNN) transmitter that implements a high-dimension modulation scheme and a CNN-based receiver that computes log-likelihood ratios (LLRs) on the transmitted bits. Both transceivers operate on top of OFDM to benefit from its efficient hardware implementation and process OFDM symbols instead of individual resource elements (REs). We derive a training procedure which allows to both maximize an achievable information rate and to offset OFDM drawbacks by defining specific optimization constraints. The end-to-end system training is performed through stochastic gradient descent (SGD), and therefore the achievable rate and the constraints need to be expressed as functions that can be evaluated and differentiated during training.

In the following, we focus on designing OFDM-based waveforms that enable pilotless transmissions and satisfy PAPR and ACLR constraints. The end-to-end system is benchmarked against a close to ideal implementation of a tone reservation (TR) baseline, in which a number of

subcarriers are used to generate peak-reduction signals. Both systems are evaluated on a 3rd Generation Partnership Project (3GPP)-compliant channel model, and the baseline uses a pilot configuration supported by the 5G new radio (NR) specifications. The end-to-end system, on the contrary, does not use any pilots and learns a high-dimensional modulation that enables accurate detection at the receiver. Evaluation results show that the learning-based system allows to meet PAPR and ACLR targets and enables throughput gains ranging from 3% to 30% compared to a baseline with similar characteristics. To get insight into how the proposed system reduces the PAPR and ACLR while maintaining high rates, we have carried out a detailed study of the learned high-dimensional modulation scheme. We have found out that ACLR and PAPR reduction is achieved through a combination of spectral filtering, uneven energy allocation across subcarriers, and positional adjustments of constellation symbols. To the best of our knowledge, this method is the first ML-based approach that jointly maximizes an information rate of OFDM transmissions and allows to set PAPR and ACLR targets.¹

Related literature

To counteract the drawbacks of OFDM-based waveforms, previous works suggested filtering the analog signal, to modify the constellation used for modulation, or to inject custom signals on reserved subcarriers. The first approach is known as iterative clipping and filtering, and iterates between clipping in the time-domain and filtering in the frequency domain to constrain the signal amplitude and possibly the spectral leakage [4]. The second scheme, named active constellation extension, extends the outer symbols of a constellation to reduce the signal PAPR at the cost of an increased power consumption [5]. Finally, the third technique reserves a subset of available subcarriers to create a peak-cancelling signal, and is referred to as tone reservation (TR) [6].

Motivated by the success of ML in other physical layer tasks, such as channel coding [7] and wireless communications [8], multiple works suggested replacing existing algorithms with ML components. For example, an NN was used to generate the constellation extension vectors in [9]. Similarly, a TR algorithm was unfolded as NN layers in [10]–[12]. It has also been proposed to model the communication system as an autoencoder that is trained to both minimize the PAPR and symbol error rate [13]. Although closer to our approach, the proposed scheme operates on symbols, meaning that the bit mapping and demapping have to be implemented

¹Part of this work has been published in [3].

separately, and has only been evaluated on a simple Rayleigh fading channel. Moreover, the time-domain signal is not oversampled, which is required to obtain an accurate representation of the underlying waveform for PAPR calculations [14]. Finally, none of these works allow setting precise PAPR and ACLR targets, which means that the tradeoff between the PAPR, ACLR, and spectral efficiency can not be accurately controlled.

Regarding the end-to-end training of communication systems, numerous works proposed to leverage this technique to design transceivers aimed at different channels. For example, the design of constellation geometries to achieve pilotless and cyclic prefix (CP)-less communication over OFDM channels was studied in [15], while the design of transmit and receive filters for single-carrier systems under spectral and PAPR constraints was presented in [16]. Other works in similar directions include the design of a deep learning (DL)-aided multicarrier system for fading channels [17] and the design of NN-based transceivers for optical fiber communications [18].

Notations : \mathbb{R} (\mathbb{C}) denotes the set of real (complex) numbers. Tensors and matrices are denoted by bold upper-case letters and vectors are denoted by bold lower-case letters. We respectively denote by \mathbf{m}_a and $m_{a,b}$ the vector and scalar formed by slicing the matrix \mathbf{M} along its first and second dimension. $(\cdot)^\top$, $(\cdot)^H$, and $(\cdot)^*$ denote the transpose, conjugate transpose, and element-wise conjugate operator, respectively. We denote by \odot and \oslash the element-wise multiplication and division operator, also known as Hadamard product and division. $I(\mathbf{x}; \mathbf{y})$ and $P(\mathbf{x}, \mathbf{y})$ respectively represent the mutual information and joint conditional probability of \mathbf{x} and \mathbf{y} . Finally, the imaginary unit is denoted by j , such that $j^2 = -1$.

II. PROBLEM STATEMENT

A single-input single-output (SISO) system using OFDM is considered. In this section, the OFDM channel model is first presented, and the expressions of the signal waveform and spectrum are derived. The ACLR and PAPR metrics typically used to characterize the analogue signal are then detailed. Finally, a close to ideal implementation of a TR baseline is introduced, where a subset of subcarriers are reserved to minimize the signal PAPR and pilots are transmitted to estimate the channel.

A. System model

1) *Channel model:* Signals are transmitted over N subcarriers and one time slot, which consists of $M = 14$ adjacent OFDM symbols. Each time-frequency position is called an RE and

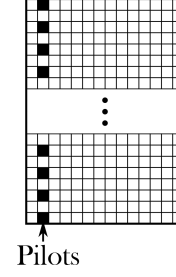
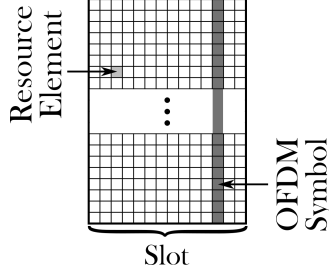


Fig. 1: The frequency-time resource grid. Fig. 2: Pilot pattern used by the baseline.

the entire grid is referred to as the resource grid (RG), as depicted in Fig 1. The subcarriers are indexed by the set $\mathcal{N} = \{-\frac{N-1}{2}, \dots, \frac{N-1}{2}\}$, with N assumed odd for convenience. When using a CP, the OFDM channel can be expressed as

$$\mathbf{Y} = \mathbf{H} \odot \mathbf{X} + \mathbf{N} \quad (1)$$

where $\mathbf{X} \in \mathbb{C}^{M \times N}$ and $\mathbf{Y} \in \mathbb{C}^{M \times N}$ respectively represent the matrix of sent and received frequency baseband symbols (FBSs), $\mathbf{H} \in \mathbb{C}^{M \times N}$ is the matrix of channel coefficients, and $\mathbf{N} \in \mathbb{C}^{M \times N}$ is the additive Gaussian noise matrix such that each element has a variance σ^2 . We consider a slow-varying environment so that the channel can be assumed constant over the duration of a slot. The matrix of bits to be transmitted on the OFDM symbol m is denoted $\mathbf{B}_m = [\mathbf{b}_{m,1}, \dots, \mathbf{b}_{m,N}]^T$, where $\mathbf{b}_{m,n} \in \{0, 1\}^K$, $1 \leq m \leq M$, $1 \leq n \leq N$, is a vector of bits to be sent and K is the number of bits per channel use. The transmitter modulates each \mathbf{B}_m onto the FBSs $\mathbf{x}_m \in \mathbb{C}^N$, which are mapped on the orthogonal subcarriers to form the spectrum

$$S_m(f) = \sum_{n \in \mathcal{N}} x_{m,n} \frac{1}{\sqrt{\Delta_f}} \text{sinc} \left(\frac{f}{\Delta_f} - n \right) \quad (2)$$

where Δ_f is the subcarrier spacing. The corresponding time-domain signal is

$$s_m(t) = \sum_{n \in \mathcal{N}} x_{m,n} \frac{1}{\sqrt{T}} \text{rect} \left(\frac{t}{T} - m \right) e^{i2\pi n \frac{t-mT}{T}} \quad (3)$$

where $T = \frac{1}{\Delta_f}$ is the duration of an OFDM symbol without CP. To avoid intersymbol interference in multipath fading channels, CPs of durations at least equal to the longest path need to be inserted. If we denote by T^{CP} the length of this CP, the transmitted signal is expressed as

$$s_m^{\text{CP}}(t) = \begin{cases} \frac{\sqrt{T}}{\sqrt{T+T^{\text{CP}}}} s_m(t - mT^{\text{CP}}) & \text{if } t \bmod T + T^{\text{CP}} \geq T_{\text{CP}} \\ \frac{\sqrt{T}}{\sqrt{T+T^{\text{CP}}}} s_m(t - mT^{\text{CP}} + T) & \text{if } t \bmod T + T^{\text{CP}} < T_{\text{CP}} \end{cases} \quad (4)$$

which is normalized so that the average energy per FBS is one. The baseband spectrum of the transmitted signal (with CP) is therefore

$$S_m^{\text{CP}}(f) = \sum_{n \in \mathcal{N}} x_{m,n} \frac{1}{\sqrt{\Delta_f^{\text{CP}}}} \text{sinc} \left(\frac{f - n\Delta_f}{\Delta_f^{\text{CP}}} \right) \quad (5)$$

where $\Delta_f^{\text{CP}} = \frac{1}{T+T^{\text{CP}}}$.

2) *Relevant metrics:* OFDM waveforms have, inter alia, two major drawbacks. The first one is their high amplitude peaks, which create distortions in the output signal due to PA saturation. Such distortions are usually reduced by operating the PA with a large power back-off or by leveraging complex digital pre-distortion, thus reducing the power efficiency. Let us denote by $\alpha(t) = \frac{|s(t)|^2}{\mathbb{E}[|s(t)|^2]}$ the ratio between the instantaneous and average power of a signal. We define the PAPR_ϵ as the smallest $e \geq 0$, such that the probability of α being larger than e is smaller than a threshold $\epsilon \in (0, 1)$:

$$\text{PAPR}_\epsilon := \min e, \text{ s. t. } P(\alpha(t) > e) \leq \epsilon. \quad (6)$$

Setting $\epsilon = 0$ leads to the more conventional PAPR definition $\frac{\max |s(t)|^2}{\mathbb{E}[|s(t)|^2]}$. However, the maximum signal power occurs with very low probability, and therefore such a definition of the PAPR only has a limited practical interest. Relaxing ϵ to values greater than 0 allows considering more frequent, and therefore more practically relevant, power peaks.

The second drawback of OFDM is its low spectral containment. This characteristic is typically measured with the ACLR, which is the ratio between the expected out-of-band energy $\mathbb{E}_{\mathbf{x}_m}[E_{O_m}]$ and the expected in-band energy $\mathbb{E}_{\mathbf{x}_m}[E_{I_m}]$:

$$\text{ACLR} := \frac{\mathbb{E}_{\mathbf{x}_m}[E_{O_m}]}{\mathbb{E}_{\mathbf{x}_m}[E_{I_m}]} = \frac{\mathbb{E}_{\mathbf{x}_m}[E_{A_m}]}{\mathbb{E}_{\mathbf{x}_m}[E_{I_m}]} - 1 \quad (7)$$

where E_{O_m} , E_{I_m} , and $E_{A_m} = E_{O_m} + E_{I_m}$ are respectively the out-of-band, in-band, and total energy of the OFDM symbol m . The in-band energy E_{I_m} is given by

$$E_{I_m} := \int_{-\frac{N\Delta_f}{2}}^{\frac{N\Delta_f}{2}} |S_m(f)|^2 df = \mathbf{x}_m^H \mathbf{V} \mathbf{x}_m \quad (8)$$

where each element $v_{a,b}$ of the matrix $\mathbf{V} \in \mathbb{R}^{N \times N}$ is

$$v_{a,b} = \frac{1}{\Delta_f^{\text{CP}}} \int_{-\frac{N\Delta_f}{2}}^{\frac{N\Delta_f}{2}} \text{sinc} \left(\frac{f - a\Delta_f}{\Delta_f^{\text{CP}}} \right) \text{sinc} \left(\frac{f - b\Delta_f}{\Delta_f^{\text{CP}}} \right) df, \quad a, b \in \mathcal{N}. \quad (9)$$

The effect on the CP length on the in-band energy is shown in Fig.3, which have been obtained by sending 10^6 random FBSs $\mathbf{x}_m \sim \mathcal{CN}(\mathbf{0}, \frac{1}{\sqrt{2}}\mathbf{I})$ on $N = 25$ subcarriers with CP lengths of

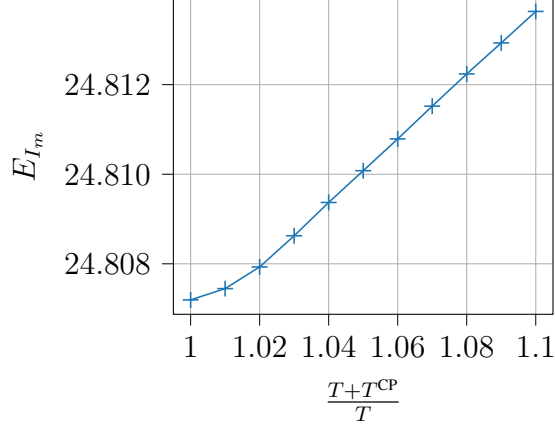


Fig. 3: Effect of the CP length on the in-band energy.

$T^{\text{CP}} \in [0, 0.1T]$. It can be seen that the in-band energy increases with the CP length, which is to be expected as increasing T^{CP} amounts to modulating the subcarriers with sinc for which the ripples are brought closer together, thus containing more energy in $[\Delta_f(n - \frac{1}{2}), \Delta_f(n + \frac{1}{2})]$. This in-band energy increase can be directly mapped to an ACLR decrease, as the total energy does not depend on CP length. In the following, we therefore consider that $T^{\text{CP}} = 0$ when computing the time-domain representation and spectrum of the signal, as it corresponds to the worst-case scenario in terms of spectral energy leakage.

Finally, the total energy can be more conveniently computed in the time domain:

$$E_{A_m} := \int_{-\frac{T}{2}}^{\frac{T}{2}} |s(t)|^2 dt = \mathbf{x}_m^H \mathbf{W} \mathbf{x}_m \quad (10)$$

where $\mathbf{W} \in \mathbb{R}^{N \times N}$ has elements

$$w_{a,b} = \frac{1}{T} \int_{-\frac{T}{2}}^{\frac{T}{2}} e^{i2\pi(a-b)t/T} dt, \quad a, b \in \mathcal{N}. \quad (11)$$

B. Baseline

One technique to reduce the PAPR of OFDM signal is TR, in which a subset of R tones (subcarriers) is used to create peak-reduction signals. These subcarriers are referred to as peak reduction tones (PRTs), and the remaining D subcarriers are used for data and pilot transmission. The sets containing the PRTs and the data-carrying subcarriers are respectively denoted by \mathcal{R} and \mathcal{D} , and are such that $\mathcal{R} \cup \mathcal{D} = \mathcal{N}$.

1) *Transmitter*: The TR-based transmitter sends three types of signals: data signals, peak reduction signals, and pilot signals which are used by the receiver to estimate the channel. Such pilots are inserted in the RG following the 5G NR pattern visible in Fig. 2, i.e., every two REs on the second OFDM symbol, and the value of each pilot is chosen randomly on the unit circle. For clarity, only data and peak-reduction signals are considered when describing the transmitter, as transmitting pilots is achieved by simply replacing some REs carrying data by reference signals. We denote by $u_{m,n \in \mathcal{D}}$ and $c_{m,n \in \mathcal{R}}$ the FBSs carrying data and peak-reduction signals, respectively. An FBS $u_{m,n \in \mathcal{D}}$ corresponds to the mapping of a vector of bits $\mathbf{b}_{m,n \in \mathcal{D}}$ following a 2^K -quadrature amplitude modulation (QAM), the constellation of which is denoted by $\mathcal{C} \in \mathbb{C}^{2^K}$. The vector of FBSs $\mathbf{u}_m \in \mathbb{C}^N$ is composed of all $u_{m,n \in \mathcal{D}}$ and of zeros at positions that correspond to PRTs, i.e., $u_{m,n \in \mathcal{R}} = 0$. The reduction vector $\mathbf{c}_m \in \mathbb{C}^N$ is formed by the signals $c_{m,n \in \mathcal{R}}$ mapped to the PRTs, and is conversely such that $c_{m,n \in \mathcal{D}} = 0$. As an example, if three subcarriers are used and only the last one is used as a PRT, these vectors are expressed as $\mathbf{u}_m = [u_{m,-1}, u_{m,0}, 0]^\top$ and $\mathbf{c}_m = [0, 0, c_{m,1}]^\top$. The vector of discrete baseband signals to be transmitted and the corresponding continuous-time waveform are finally denoted by $\mathbf{x}_m = \mathbf{u}_m + \mathbf{c}_m$ and $s_m(t)$, respectively. TR aims at finding \mathbf{c}_m that minimizes the maximum squared signal amplitude, i.e.,

$$\arg \min_{\mathbf{c}_m} \max_t |s_m(t)|^2. \quad (12)$$

As minimization over the time-continuous signal leads to intractable calculations, $s_m(t)$ is first discretized. Many previous studies considered a discrete vector $\mathbf{z}_m \in \mathbb{C}^N$, sampled with a period $\frac{T}{N}$, as a substitute for the underlying signal [11]–[13]. However, it has been shown that using a vector $\underline{\mathbf{z}}_m \in \mathbb{C}^{NO_s}$, oversampled by a factor O_s , is necessary to correctly represent the analog waveform [14]. The difference between the two discretized vectors are visible in Fig. 4, where the squared amplitude of \mathbf{z}_m and $\underline{\mathbf{z}}_m$ are plotted for an arbitrary OFDM symbol, with $N = 75$ subcarriers and an oversampling factor of $O_s = 5$. It can be seen that the oversampled signal exhibits a different maximum peak with a higher amplitude as well as numerous secondary peaks that are not present in the non-oversampled signal. These peaks might lie in the PA saturation region, causing distortions of the transmitted waveform. Let us define the inverse discrete Fourier transform (IDFT) matrix $\mathbf{F}^H \in \mathbb{C}^{NO_s \times N}$, where each element is expressed as $f_{a,b} = \frac{1}{\sqrt{NO_s}} e^{j\frac{2\pi ab}{NO_s}}$. The oversampled vector can be obtained with

$$\underline{\mathbf{z}}_m = \mathbf{F}^H \mathbf{x}_m = \mathbf{F} (\mathbf{u}_m + \mathbf{c}_m). \quad (13)$$

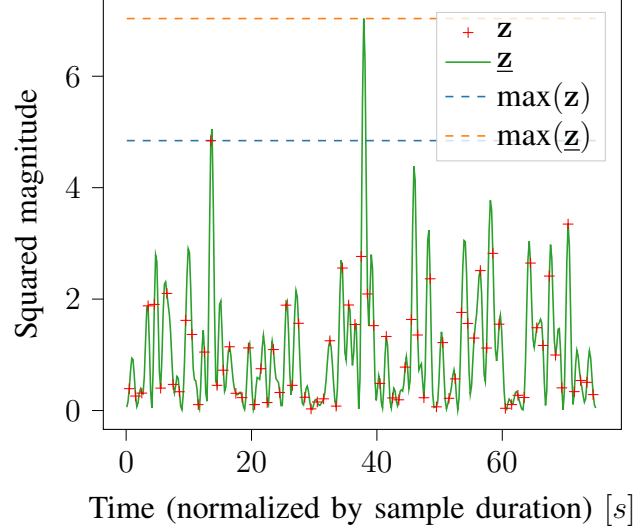


Fig. 4: OFDM signal generated from $N = 75$ subcarriers.

The value of \mathbf{c}_m that minimizes the PAPR can now be approximately found by minimizing the oversampled signal:

$$\arg \min_{\mathbf{c}_m} \|g(\mathbf{F}^H(\mathbf{u}_m + \mathbf{c}_m))\|_{\infty} \quad (14)$$

where $g(\cdot)$ denotes the element-wise squared magnitude $|\cdot|^2$ and $\|\cdot\|_{\infty}$ denotes the infinity norm. The convexity of $\|g(\mathbf{F}(\mathbf{u}_m + \mathbf{c}_m))\|_{\infty}$ theoretically allows to find the optimal value of \mathbf{c}_m , but the associated complexity leads to the development of algorithms that approximate this value in a limited number of iterations [6]. In this work, however, we use a convex solver [19] to find the exact solution of (14) for each symbol \mathbf{x}_m . Although such a scheme would be prohibitively complex in practice, it is considered here to provide a close to ideal implementation of a TR-based baseline. Moreover, for fairness with conventional QAM systems, we add the convex constraint $\mathbf{c}_m^H \mathbf{c}_m \leq R$ so that the average energy per OFDM symbol equals at most N . We experimentally verified that the average energy of the peak reduction signals $\mathbb{E}_{\mathbf{c}_m} [\mathbf{c}_m^H \mathbf{c}_m]$ was always close to R , leading to $\mathbb{E}_{\mathbf{x}_m} [\mathbf{x}_m^H \mathbf{x}_m] \approx N$. Finally, it was shown that placing the PRTs at random locations at every transmission leads to the lowest PAPR among other placement techniques [20]. The baseline therefore implements such a random positioning scheme for all OFDM symbols, except for the one carrying pilots for which peak-reduction signals cannot be inserted on pilot-carrying subcarriers. On this specific OFDM symbol, the number of PRTs is also reduced to $\frac{R}{2}$ in order to always maintain a significant number of subcarriers carrying data.

2) *Receiver*: On the receiver side, channel estimation is performed first, using the pilot signals received in the pilot-carrying OFDM symbol $m^{(p)} \in \mathcal{M}$. The pattern depicted in Fig. 2 allocates $\frac{N+1}{2}$ REs to pilot transmissions. Let us denote by $\mathbf{p}_{m^{(p)}} \in \mathbb{C}^{\frac{N+1}{2}}$ the vector of received pilot signals, extracted from $\mathbf{y}_{m^{(p)}}$. The channel covariance matrix, providing the spectral correlations between all REs carrying pilots, is denoted by $\Sigma \in \mathbb{C}^{\frac{N+1}{2} \times \frac{N+1}{2}}$. This matrix can be empirically estimated by constructing a large dataset of received pilot signals and computing the statistics over the entire dataset. The channel coefficients at REs carrying pilots are estimated using linear minimum mean squared error (LMMSE):

$$\hat{\mathbf{h}}_{m^{(p)}}^{(p)} = \Sigma \left(\Sigma + \sigma^2 \mathbf{I}_{\frac{N+1}{2}} \right)^{-1} \mathbf{p}_{m^{(p)}} \in \mathbb{C}^{\frac{N+1}{2}}. \quad (15)$$

Channel estimation at the remaining N REs of the OFDM symbol $m^{(p)}$ is achieved through linear interpolation. As the channel is assumed to be invariant over the duration of a slot, the so obtained vector $\hat{\mathbf{h}}_{m^{(p)}} \in \mathbb{C}^N$ is also used for all other OFDM symbols, forming the channel estimate matrix $\hat{\mathbf{H}} \in \mathbb{C}^{M \times N}$ where all columns are equal. On fast changing channels, pilots could be inserted in other OFDM symbols to better track the evolution of the channel.

The transmitted FBSs are estimated through equalization:

$$\hat{\mathbf{X}} = \mathbf{Y} \oslash \hat{\mathbf{H}}. \quad (16)$$

Finally, the LLR of the k^{th} bit corresponding to the RE (m, n) is computed with a conventional additive white Gaussian noise (AWGN) demapper:

$$\text{LLR}_{m,n}(k) = \ln \left(\frac{\sum_{c \in \mathcal{C}_{k,1}} \exp \left(-\frac{|\hat{h}_{m,n}|^2}{\sigma^2} |\hat{x}_{m,n} - c|^2 \right)}{\sum_{c \in \mathcal{C}_{k,0}} \exp \left(-\frac{|\hat{h}_{m,n}|^2}{\sigma^2} |\hat{x}_{m,n} - c|^2 \right)} \right) \quad (17)$$

where $\mathcal{C}_{k,1}$ ($\mathcal{C}_{k,0}$) is the subset of \mathcal{C} containing the symbols that have the k^{th} bit set to 1 (0), and $\frac{|\hat{h}_{m,n}|^2}{\sigma^2}$ is the post-equalization noise variance.

III. LEARNING A HIGH DIMENSIONAL MODULATION

In the following, we train an NN-based transmitter and receiver to maximize an achievable rate under ACLR and PAPR constraints. This end-to-end system is referred to as "E2E" system for brevity, and is schematically shown in Fig. 5. An optimization procedure is derived to handle the constrained optimization problem, in which the loss function is expressed as a differentiable augmented Lagrangian. Next, we detail the transmitter and receiver architectures, both implemented as CNNs.

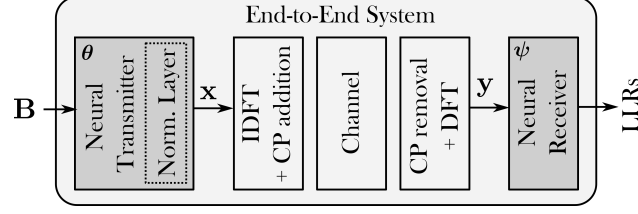


Fig. 5: Trainable system, where grayed blocks represent trainable components.

A. Optimization procedure

1) *Problem formulation:* We aim at finding a high-dimensional modulation and associated detector that both maximize an information rate for the OFDM transmission and satisfy constraints on the signal PAPR and ACLR. The transmitter and receiver of the E2E system operate on top of OFDM, i.e., IDFT (DFT) is performed and a cyclic prefix is added (removed) before (after) transmission (see Fig. 5). The considered rate [15] depends on the transmitter and receiver trainable parameters, respectively denoted by θ and ψ , and is achievable assuming a bit metric decoder [21]:

$$C(\theta, \psi) = \frac{1}{MN} \sum_{m \in \mathcal{M}} \sum_{n \in \mathcal{N}} \sum_{k=0}^{K-1} I(b_{m,n,k}; \mathbf{y}_m | \theta) \quad (18)$$

$$- \frac{1}{MN} \sum_{m \in \mathcal{M}} \sum_{n \in \mathcal{N}} \sum_{k=0}^{K-1} \mathbb{E}_{\mathbf{y}_m} \left[\text{D}_{\text{KL}} \left(P(b_{m,n,k} | \mathbf{y}_m) || \hat{P}_{\psi}(b_{m,n,k} | \mathbf{y}_m) \right) \right].$$

The first term in (18) is the sum of the mutual informations between all $b_{m,n,k}$ and \mathbf{y}_m , and corresponds to an achievable information rate assuming an ideal receiver that computes the true posterior distributions $P(b_{m,n,k} | \mathbf{y}_m)$. The second term is the sum of the expected values of the Kullback–Leibler divergences between the estimated posterior probabilities $\hat{P}_{\psi}(b_{m,n,k} | \mathbf{y}_m)$ and the true ones $P(b_{m,n,k} | \mathbf{y}_m)$, and corresponds to a rate loss due to the suboptimal receiver [15]. It can be seen as a measure of distance between the probabilities that would be computed by an ideal receiver and the ones estimated by our NN-based implementation. As the E2E system directly outputs LLRs, the estimated posterior probabilities can be obtained from

$$\text{LLR}_{m,n}(k) := \ln \left(\frac{\hat{P}_{\psi}(b_{m,n,k} = 1 | \mathbf{y}_m)}{\hat{P}_{\psi}(b_{m,n,k} = 0 | \mathbf{y}_m)} \right). \quad (19)$$

To ensure a unit average energy per RE, a normalization layer is added to the transmitter (see Fig. 5). Perfect normalization would perform

$$l_{\text{norm}}^*(\mathbf{x}_m) = \frac{\mathbf{x}_m}{\left(\frac{1}{N} \mathbb{E}_{\mathbf{x}_m}[E_{A_m}]\right)^{\frac{1}{2}}} \quad (20)$$

but the 2^{MNK} different combinations of bits would make the computation of the expected value too complex for any practical system. Batch normalization is therefore preferred, ensuring that the average energy per RE in the batch is one:

$$l_{\text{norm}}(\mathbf{x}_m^{[j]}) = \frac{\mathbf{x}_m^{[j]}}{\left(\frac{1}{MNB_s} \sum_{m \in \mathcal{M}} \sum_{i=1}^{B_s} \mathbf{x}_m^{[i]\text{H}} \mathbf{W} \mathbf{x}_m^{[i]}\right)^{\frac{1}{2}}} \quad (21)$$

where the superscript $[j]$ denotes the j^{th} element in the batch. This expression is slightly different from the one typically used in related works, since it accounts for the correlation that can appear between the FBSs generated by the transmitter. Conventional bit-interleaved modulation systems produces independent and identically distributed (i.i.d.) symbols, and therefore does not need to take such correlation into account.

We can now formulate the constrained optimization problem we aim to solve:

$$\underset{\boldsymbol{\theta}, \boldsymbol{\psi}}{\text{maximize}} \quad C(\boldsymbol{\theta}, \boldsymbol{\psi}) \quad (22a)$$

$$\text{subject to} \quad \text{PAPR}_\epsilon(\boldsymbol{\theta}) = \gamma_{\text{peak}} \quad (22b)$$

$$\text{ACLR}(\boldsymbol{\theta}) \leq \beta_{\text{leak}} \quad (22c)$$

where γ_{peak} and β_{leak} respectively denote the target PAPR and ACLR. Note that the PAPR and ACLR depend on the transmitter parameters $\boldsymbol{\theta}$.

2) *System training*: One of the main advantages of implementing the transmitter-receiver pair as an E2E system is that it enables optimization of the trainable parameters through SGD. This requires a differentiable loss function so that the gradients can be computed and backpropagated through the E2E system. In the following, the augmented Lagrangian method is leveraged to convert the problem (22) into its augmented Lagrangian, which acts a differentiable loss function that can be minimized with respect to $\boldsymbol{\theta}$ and $\boldsymbol{\psi}$ [22]. The key idea is to relax the constrained optimization problem into a sequence of unconstrained problems that are solved iteratively. This method is known to be more effective than the quadratic penalty method, enabling a faster and more stable convergence [23]. In the following, we express the objective (22a) and the constraints

(22b) and (22c) as differentiable functions that can be evaluated during training and minimized with SGD.

First, the achievable rate (22a) can be equivalently expressed using the system binary cross-entropy (BCE) [24], which is widely used in binary classification problems:

$$L_C(\boldsymbol{\theta}, \boldsymbol{\psi}) := -\frac{1}{MN} \sum_{m \in \mathcal{M}} \sum_{n \in \mathcal{N}} \sum_{k=0}^{K-1} \mathbb{E}_{\mathbf{y}_m} \left[\log_2 \left(\hat{P}_{\boldsymbol{\psi}}(b_{m,n,k} | \mathbf{y}_m) \right) \right] \quad (23)$$

$$= K - C(\boldsymbol{\theta}, \boldsymbol{\psi}). \quad (24)$$

To overcome the complexity associated with the computation of the expected value, an approximation is typically obtained through Monte Carlo sampling:

$$L_C(\boldsymbol{\theta}, \boldsymbol{\psi}) \approx -\frac{1}{MNB_s} \sum_{m \in \mathcal{M}} \sum_{n \in \mathcal{N}} \sum_{k=0}^{K-1} \sum_{i=0}^{B_s-1} \log_2 \left(\hat{P}_{\boldsymbol{\psi}} \left(b_{m,n,k}^{[i]} | \mathbf{y}_m^{[i]} \right) \right). \quad (25)$$

Second, evaluating the constraint (22b) requires the computation of the probability $P(\frac{|s(t)|^2}{\mathbb{E}[|s(t)|^2]} > e)$, where e is the energy threshold defined in (6). However, computing such probability would be prohibitively complex due to the sheer amount of possible OFDM symbols. During training, we therefore enforce the constraint by setting $\epsilon = 0$ and penalizing all signals whose squared amplitude exceed γ_{peak} . With $\epsilon = 0$, the constraint (22b) is equivalent to enforcing $L_{\gamma_{\text{peak}}}(\boldsymbol{\theta}) = 0$, with

$$L_{\gamma_{\text{peak}}}(\boldsymbol{\theta}) = \mathbb{E}_m \left[\int_{-\frac{T}{2}}^{\frac{T}{2}} (|s_m(t)|^2 - \gamma_{\text{peak}})^+ dt \right] \quad (26)$$

where $(x)^+$ denotes the positive part of x , i.e., $(x)^+ = \max(0, x)$. To evaluate $L_{\gamma_{\text{peak}}}(\boldsymbol{\theta})$ during training, the value of the expectation can be obtained through Monte Carlo sampling, and the integral can be approximated using a Riemann sum:

$$L_{\gamma_{\text{peak}}}(\boldsymbol{\theta}) \approx \frac{T}{B_s NO} \sum_{i=0}^{B_s-1} \sum_{t=-\frac{NO_s-1}{2}}^{\frac{NO_s-1}{2}} \left(\left| \underline{z}_{m,t}^{[i]} \right|^2 - \gamma_{\text{peak}} \right)^+ \quad (27)$$

where $\underline{z}_m = \mathbf{F}^{-1} \mathbf{x}_m \in \mathbb{C}^{NO_s}$ is the vector of the oversampled time signal corresponding to the neural transmitter output \mathbf{x}_m .

Third, the inequality constraint (22c) can be converted to the equality constraint $\text{ACLR}(\boldsymbol{\theta}) - \beta_{\text{leak}} = -q$, where $q \in \mathbb{R}_+$ is a positive slack variable. This equality constraint is then enforced by minimizing $L_{\beta_{\text{leak}}}(\boldsymbol{\theta}) + q$, with

$$L_{\beta_{\text{leak}}}(\boldsymbol{\theta}) = \frac{\mathbb{E}[E_A]}{\mathbb{E}[E_I]} - 1 - \beta_{\text{leak}} \quad (28)$$

$$\approx \frac{\frac{1}{B_s} \sum_{i=0}^{B_s-1} \mathbf{x}^{[i]\text{H}} \mathbf{W} \mathbf{x}^{[i]}}{\frac{1}{B_s} \sum_{i=0}^{B_s-1} \mathbf{x}^{[i]\text{H}} \mathbf{V} \mathbf{x}^{[i]}} - 1 - \beta_{\text{leak}}. \quad (29)$$

Finally, for $\epsilon = 0$, the problem (22) can be reformulated as

$$\underset{\boldsymbol{\theta}, \boldsymbol{\psi}}{\text{minimize}} \quad L_C(\boldsymbol{\theta}, \boldsymbol{\psi}) \quad (30a)$$

$$\text{subject to} \quad L_{\gamma_{\text{peak}}}(\boldsymbol{\theta}) = 0 \quad (30b)$$

$$L_{\beta_{\text{leak}}}(\boldsymbol{\theta}) + q = 0 \quad (30c)$$

where the objective and the constraints are differentiable and can be estimated at training. The augmented Lagrangian method introduces two types of hyperparameters that are iteratively updated during training. The first one corresponds to the penalty parameters which are slowly increased to penalize the constraint with increasing severity. The second one corresponds to estimates of the Lagrange multipliers, as defined in [22]. Let us denote by $\mu_p > 0$ and $\mu_l > 0$ the penalty parameters and by λ_p and λ_l the Lagrange multipliers for the constraint functions $L_{\gamma_{\text{peak}}}(\boldsymbol{\theta})$ and $L_{\beta_{\text{leak}}}(\boldsymbol{\theta})$, respectively. The corresponding augmented Lagrangian is defined as [22]

$$\begin{aligned} \bar{L}^*(\boldsymbol{\theta}, \boldsymbol{\psi}, \lambda_p, \lambda_l, \mu_p, \mu_l, q) &= L_C(\boldsymbol{\theta}, \boldsymbol{\psi}) \\ &+ \lambda_p L_{\gamma_{\text{peak}}}(\boldsymbol{\theta}) + \frac{1}{2} \mu_p |L_{\gamma_{\text{peak}}}(\boldsymbol{\theta})|^2 \\ &+ \lambda_l (L_{\beta_{\text{leak}}}(\boldsymbol{\theta}) + q) + \frac{1}{2} \mu_l |L_{\beta_{\text{leak}}}(\boldsymbol{\theta}) + q|^2. \end{aligned} \quad (31)$$

As derived in [22], the minimization of (31) with respect to q can be carried out explicitly for each fixed pair of $\{\boldsymbol{\theta}, \boldsymbol{\psi}\}$ so that the augmented Lagrangian can be equivalently expressed as

$$\begin{aligned} \bar{L}(\boldsymbol{\theta}, \boldsymbol{\psi}, \lambda_p, \lambda_l, \mu_p, \mu_l) &= L_C(\boldsymbol{\theta}, \boldsymbol{\psi}) \\ &+ \lambda_p L_{\gamma_{\text{peak}}}(\boldsymbol{\theta}) + \frac{1}{2} \mu_p |L_{\gamma_{\text{peak}}}(\boldsymbol{\theta})|^2 \\ &+ \frac{1}{2\mu_l} (\max(0, \lambda_l + \mu_l L_{\beta_{\text{leak}}}(\boldsymbol{\theta}))^2 - \lambda_l^2). \end{aligned} \quad (32)$$

Each training iteration comprises multiples steps of SGD on the augmented Lagrangian (32) followed by an update of the hyperparameters. The optimization procedure is detailed in

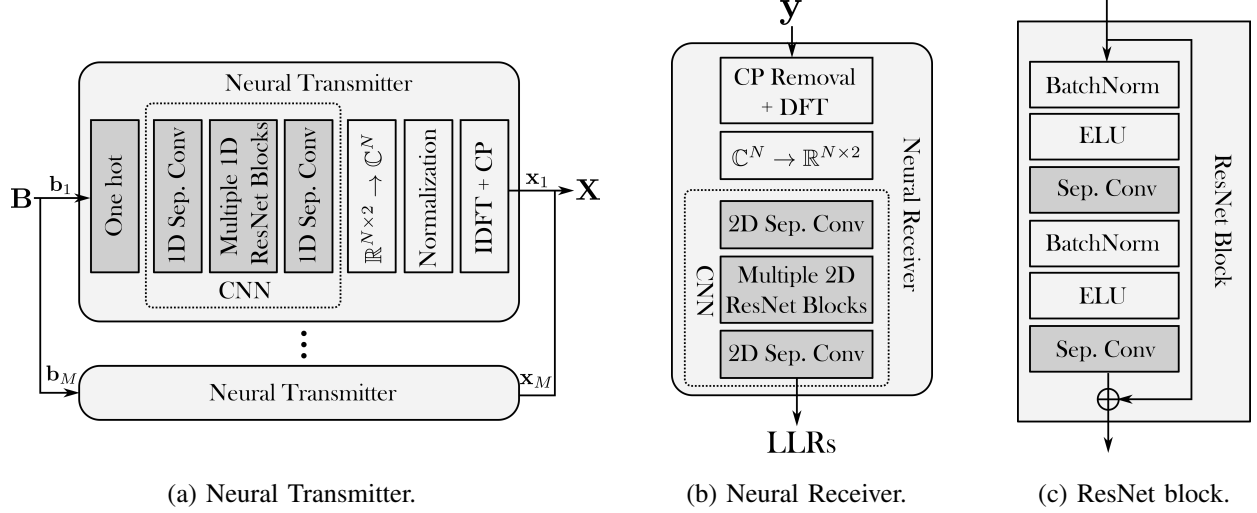


Fig. 6: Different parts of the end-to-end system, where grayed blocks are trainable components.

Algorithm 1, where $\tau \in \mathbb{R}^+$ controls the evolution of the penalty parameters and the superscript (u) refers to the u^{th} iteration of the algorithm.

Algorithm 1: Training procedure

Initialize $\theta, \psi, \lambda_p^{(0)}, \lambda_l^{(0)}, \mu_p^{(0)}, \mu_l^{(0)}$

for $u = 0, \dots$ **do**

▷ Perform multiple steps of SGD

on $\bar{L}(\theta, \psi, \lambda, \lambda_l, \mu_p, \mu_l)$ w.r.t. θ and ψ

▷ Update optimization hyperparameters:

$$\lambda_p^{(u+1)} = \lambda_p^{(u)} + \mu_p^{(u)} L_{\gamma_{\text{peak}}}(\theta)$$

$$\lambda_l^{(u+1)} = \max \left(0, \lambda_l^{(u)} + \mu_l^{(u)} L_{\beta_{\text{leak}}}(\theta) \right)$$

$$\mu_p^{(u+1)} = (1 + \tau) \mu_p^{(u)}$$

$$\mu_l^{(u+1)} = (1 + \tau) \mu_l^{(u)}$$

end

B. System architecture

The neural transmitter and receiver are based on similar architectures, schematically shown in Fig. 6. The core element is a *ResNet block*, which was introduced in the physical layer to implement a fully NN-based radio receiver [25], and whose effectiveness has been demonstrated

in other related works [15], [26], [27]. A ResNet block is made of two identical sequences of layers followed by the addition of the input, as depicted in Fig. 6c. In the original ResNet block [28], each sequence was composed of a batch normalization layer, a rectified linear unit (ReLU) activation function, and a convolution. Our architecture differs from the original one in that ReLUs are replaced by exponential linear units (ELUs) to alleviate the vanishing gradient problem [29] and separable convolutions are used since they enable similar performance than conventional ones but at a fraction of the computational cost [30]. Finally, we use zero-padding on all 1D (2D) convolutions to maintain constant the size of the first (and possibly second) dimension(s). In the following, the architectures of the neural transmitter and receiver are detailed, although the exact numbers of parameters for each layer are given in Section IV-A.

The transmitter processes all OFDM symbols in parallel (see Fig. 6a). Each instance of the CNN implemented at the transmitter takes as input the matrix of bits \mathbf{B}_m , corresponding to the OFDM symbol m , and outputs the OFDM symbol \mathbf{x}_m . The vector of bits is first converted into its one-hot representation, i.e., into vectors of $\{0, 1\}^{2^K}$ where all elements but one are set to zero. Then, a CNN comprises one 1D separable convolution, multiple 1D ResNet blocks, and another 1D separable convolution. This CNN is fed with the one-hot matrix of dimension $N \times 2^K$, where N corresponds to the dimension of the 1D convolution and 2^K to different convolution channels, and outputs $N \times 2$ elements. The next layers convert these $N \times 2$ real numbers into N complex symbols and normalize them, as in (21), to have a unit average energy per RE. Finally, an IDFT is performed on the symbols and a CP is added before transmission. We experimentally verified that independent processing of all OFDM symbols, resulting in the use of 1D convolutions, leads to better performance than 2D convolutions that would process all OFDM symbols at once. This could be explained by the 1D nature of PAPR and ACLR measurements, which are computed for all OFDM symbols separately.

The neural receiver, on the contrary, performs a 2D processing on all OFDM symbols since it enables more accurate channel estimation and equalization [15], [27]. At reception, the CP is first removed and an DFT is applied to the received signals \mathbf{Y} . The $M \times N$ symbols are then converted into $M \times N \times 2$ real numbers that are fed, along with the transmission SNR of size $M \times N \times 1$, into a 2D CNN. The architecture of the receiver CNN is similar to the one of the transmitter, except that 2D separable convolutions are used. The last 2D separable layer outputs $M \times N \times K$ real numbers that correspond to the LLRs of all transmitted symbols, as shown in Fig. 6b. Note that no pilots are used as it was shown in [15] that pilotless communication is

	Sep. Conv. 1D (2D)	ResNet blocks 1D (2D)					Sep. Conv 1D (2D)
Kernel size	1 (1,1)	3 (3,2)	9 (9,4)	15 (15,6)	9 (9,4)	3 (3,2)	1 (1,1)
Dilation rate	1 (1,1)	1 (1,1)	2 (2,1)	4 (4,1)	2 (2,1)	1 (1,1)	1 (1,1)
# Filters	128						2 (K)

TABLE I: Parameters for the neural transmitter (receiver).

possible over OFDM channels when neural receivers are used.

IV. SIMULATIONS RESULTS AND INSIGHTS

In this section, the E2E system is benchmarked against the TR baseline. We first describe the training and evaluation setup, followed by rate, bit error rate (BER), and goodput comparisons.

A. Evaluations

1) *Training and evaluation setup:* Separate datasets were used for training and testing, both generated using a mixture of 3GPP-compliant urban microcell (UMi) line-of-sight (LOS) and non-LOS models. The channel responses were generated using QuaDRiGa 2.4.0 [31], and perfect power control was assumed such that the average channel energy per RE was one, i.e., $\mathbb{E}[|h_{m,n}|^2] = 1$. $N = 75$ subcarriers were considered with $M = 14$ OFDM symbols using CPs of sufficient lengths so that the channel can be represented by (1) in the frequency domain. The center carrier frequency and subcarrier spacing were respectively set to 3.5 GHz and 30 kHz, the number of bits per channel use was set to $K = 4$, and 16-QAM modulation was used by the baseline. Coded BER comparisons were performed using a standard 5G-compliant low-density parity-check (LDPC) code with length 1024 and rate $r = \frac{1}{2}$. The baseline was evaluated for $R \in \{0, 2, 4, 8, 16, 32\}$ PRTs and the E2E system was trained to achieve ACLR targets of $\beta_{\text{leak}} \in \{-20, -30, -40\}$ dB and PAPR targets of $\gamma_{\text{peak}} \in \{4, 5, 6, 7, 8, 9\}$ dB.

The transmitter and receiver architectures that were used are detailed in Table I. Inspired by [25], the receptive fields of the CNNs were increased using dilations, and the kernel sizes had an increasing, then decreasing number of parameters. The Lagrange multipliers were initialized to $\lambda_p^{(0)} = \lambda_l^{(0)} = 0$ and τ was set to 0.004. The penalty parameters were initialized to $\mu_p^{(0)} = 10^{-1}$

and $\mu_t^{(0)} = 10^{-3}$, which mirrors the fact that $L_{\gamma_{\text{peak}}}(\boldsymbol{\theta})$ is usually two orders of magnitude lower than $L_{\beta_{\text{leak}}}(\boldsymbol{\theta})$. The optimization procedure was composed of 2500 iterations in which 20 SGD steps were performed with a learning rate of 10^{-3} and a batch size of $B_s = 100$. The oversampling factor used to compute $\underline{\mathbf{z}}$ in (27) was set to $O_s = 5$, as it was shown to be sufficient to correctly represent the underlying analog signal [6]. Finally, the signal-to-noise ratio (SNR)

$$\text{SNR} = \frac{\mathbb{E}_{h_{m,n}} [|h_{m,n}|^2]}{\sigma^2} = \frac{1}{\sigma^2} \quad (33)$$

was chosen randomly in the interval $[10, 30]$ dB for each RG in the batch during training. The simulations parameters are listed in Table II.

Parameters	Symbol (if any)	Value
Number of OFDM symbols	M	14
Number subcarriers	N	75
Number of bits per channel use	K	4
PAPR targets	γ_{peak}	$\{4, 5, 6, 7, 8, 9\}$ dB
ACLR targets	β_{leak}	$\{-20, -30, -40\}$ dB
PRTs used by the baseline	\mathbf{R}	$\{0, 2, 4, 8, 16, 32\}$
Batch size	B_s	100 RGs
Oversampling factor	O_s	5
Center frequency (subcarrier spacing)	-	3.5 GHz (30 kHz)
Scenario	-	3GPP 38.901 UMi LOS + NLOS
SNR	-	$[10, 30]$ dB
Code length	-	1024 bit
Code rate	r	$\frac{1}{2}$
Learning rate	-	10^{-3}

TABLE II: Training and evaluation parameters.

2) *Evaluation results:* In the following evaluations, the PAPR probability threshold was set to $\epsilon = 10^{-3}$. Note that setting $\epsilon = 0$ would only take into account the maximum signal peak, which is achieved by a single possible waveform that has probability $\frac{1}{2^{NK}} \approx 10^{-90}$. The average rates per RE achieved by the baseline and the E2E systems are shown in Fig. 7, where the numbers next to the data points are the corresponding ACLRs. First, it can be seen that at the maximum

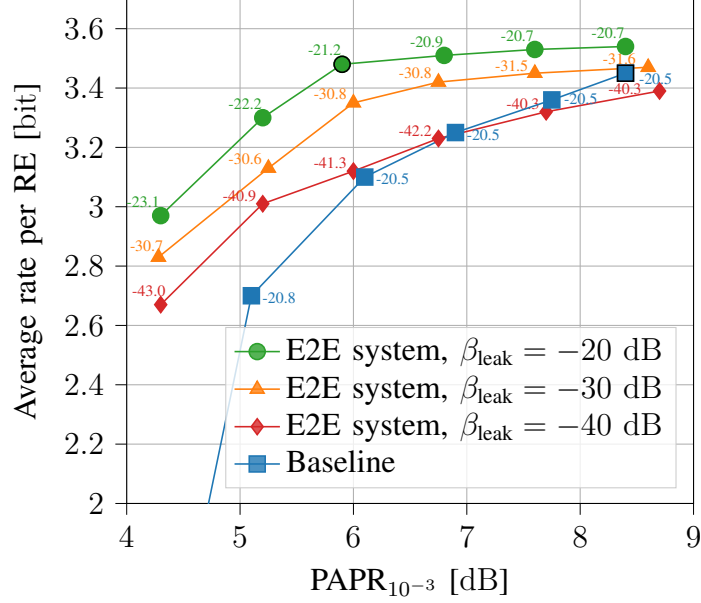


Fig. 7: Rates achieved by the compared systems. Numbers near scatter plots indicate the ACLRs.

PAPR of approximately 8.5 dB, the E2E system trained with $\beta_{leak} = -20$ dB achieves a 3% higher throughput than the baseline with no PRT. This can be explained by the rate loss due to the presence of pilots in the baseline, which do not carry data and account for approximately 4% of the total number of REs. Second, at lower PAPRs, the rates achieved by the E2E system trained with $\beta_{leak} \in \{-20, -30\}$ are significantly higher than the ones achieved by the baseline. For example, the E2E system trained with $\beta_{leak} = -20$ and $\gamma_{peak} = 5$ achieves an average rate 22% higher than the baseline for the same PAPR. Finally, the E2E systems are able to meet their respective PAPR and ACLR targets.

The coded BERs of the baseline and of the three E2E systems are shown in the left column of Fig. 8. As the baseline transmits pilots and reduction signals in addition to data signals, the energy per transmitted bit is higher than that of the E2E systems. To reflect this characteristic, we define the energy-per-bit-to-noise-spectral-density ratio as

$$\frac{E_b}{\sigma^2} = \frac{\mathbb{E}_{x_{m,n}}[|x_{m,n}|^2]}{\rho K \sigma^2} = \frac{1}{\rho K \sigma^2} \quad (34)$$

where ρ is the ratio of REs carrying data signals over the total number of REs in the RG. Fig. 8a, 8c, and 8e correspond to systems achieving PAPRs of approximately 8.5, 6.8, and 5.2 dB, respectively. Such PAPRs were obtained using $R = \{0, 4, 16\}$ PRT for the baseline, and $\gamma_{peak} = \{9, 7, 5\}$ dB for the trained systems. Note that evaluation results corresponding to

systems trained with $\beta_{\text{leak}} = \{-30, -40\}$ dB are provided for completeness, but a fair comparison is only possible between the baseline and the system trained with $\beta_{\text{leak}} = -20$ dB as this value corresponds to the baseline ACLR. Overall, one can see that the baseline consistently achieves slightly lower BER than the E2E systems. However, the baseline also transmits fewer bits per RG, due to some REs being used to transmit pilots or reduction signals.

To understand the benefits provided by the E2E approach, the second column of Fig. 8 presents the *goodputs* achieved by each compared system. The goodput is defined as the average number of information bits that have been successfully received in a RE, i.e.,

$$\text{Goodput} = r\rho K(1 - \text{BER}), \quad (35)$$

and is plotted with respect to the SNR as it already accounts for the different number of REs transmitting information bits through the parameter ρ . Evaluation results show that the goodputs achieved by all trained systems, including those trained for lower ACLRs, are significantly higher than the ones of the baseline. Indeed, at an SNR of 30 dB, all E2E systems are able to successfully transmit close to two bits per RE, while the baseline saturates at 1.93, 1.82, and 1.53 bits for PAPRs of 8.5, 6.8, and 5.2 dB, respectively. The BER improvements range from a 3% increase at low SNR with $\text{PAPR}_\epsilon \approx 8.5$ dB to a 30% increase at high SNR with $\text{PAPR}_\epsilon \approx 5.2$ dB, indicating that the E2E approach is particularly effective when the PAPR reduction is high. These gains are jointly enabled by the pilotless nature of the E2E transmission, the effective ACLR reduction scheme learned through the proposed optimization procedure, and the fact that every REs can be used to transmit data.

B. Insights on the learned ACLR and PAPR reduction techniques

1) *Interpreting the ACLR minimization process:* In order to get insight into the processing done by the neural transmitter, we first study the ACLR reduction technique learned by the E2E systems. Three covariance matrices $\mathbb{E}_{\mathbf{x}_m} [\mathbf{x}_m \mathbf{x}_m^H]$ are shown in Fig. 9 for systems trained with $\gamma_{\text{peak}} = 9$. The first covariance matrix is from a system trained with an ACLR target of $\beta_{\text{leak}} = -20$ dB, while the second and third matrices were respectively obtained with $\beta_{\text{leak}} = -30$ dB and $\beta_{\text{leak}} = -40$ dB. It can be observed that the correlation between the elements close to the diagonal increase inversely to the ACLR target. Moreover, the correlation increases at subcarriers located near the edges of the spectrum, indicating that a subcarrier-dependent filtering is learned. Fig. 10 depicts the distribution of the energy across the subcarriers. On the one hand, the system

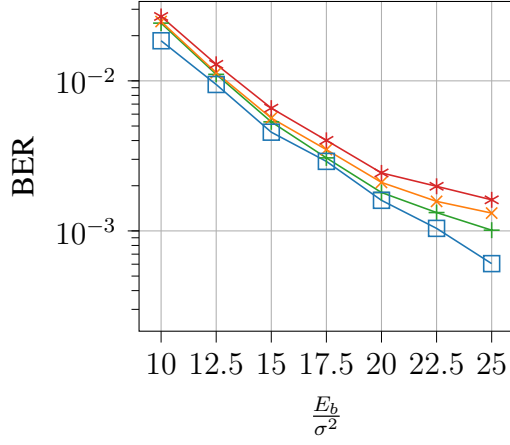
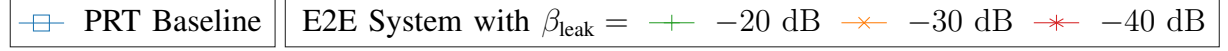
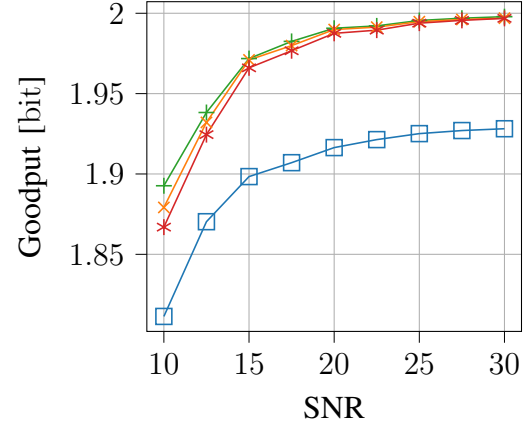
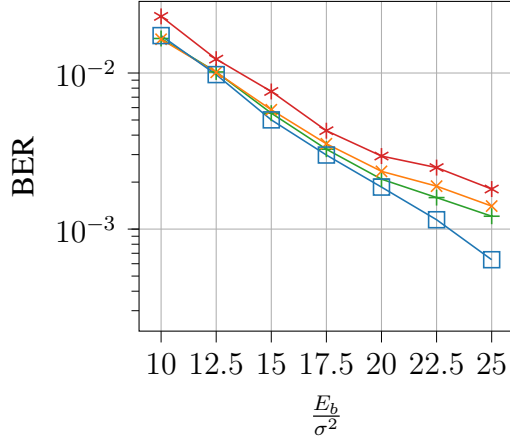
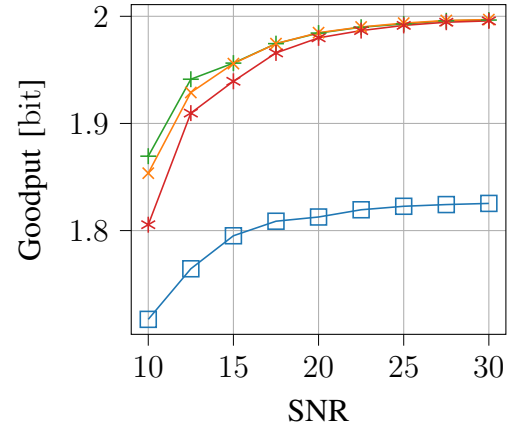
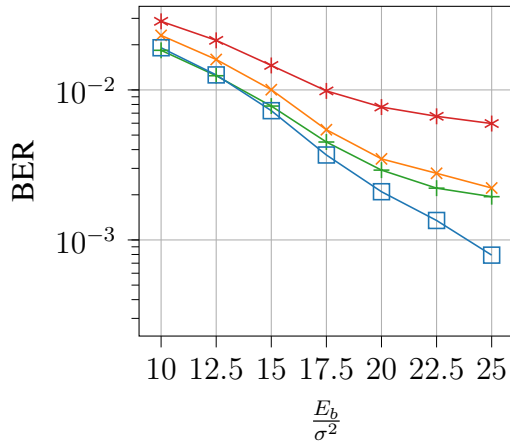
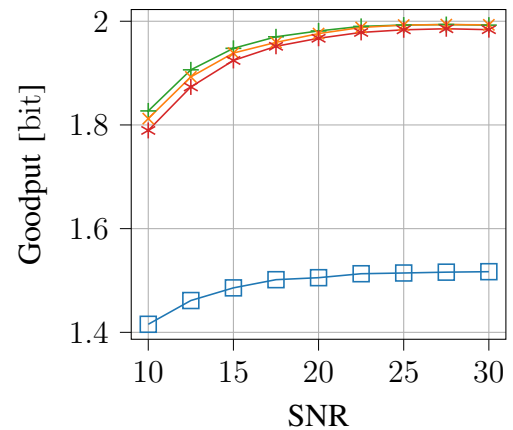
(a) Coded BER with $\gamma_{\text{peak}} = 9$ dB, $R = 0$ (b) Goodput with $\gamma_{\text{peak}} = 9$ dB, $R = 0$ (c) Coded BER with $\gamma_{\text{peak}} = 7$ dB, $R = 4$ (d) Goodput with $\gamma_{\text{peak}} = 7$ dB, $R = 4$ (e) Coded BER with $\gamma_{\text{peak}} = 5$ dB, $R = 16$ (f) Goodput with $\gamma_{\text{peak}} = 5$ dB, $R = 16$

Fig. 8: BER and goodput achieved by the different schemes.

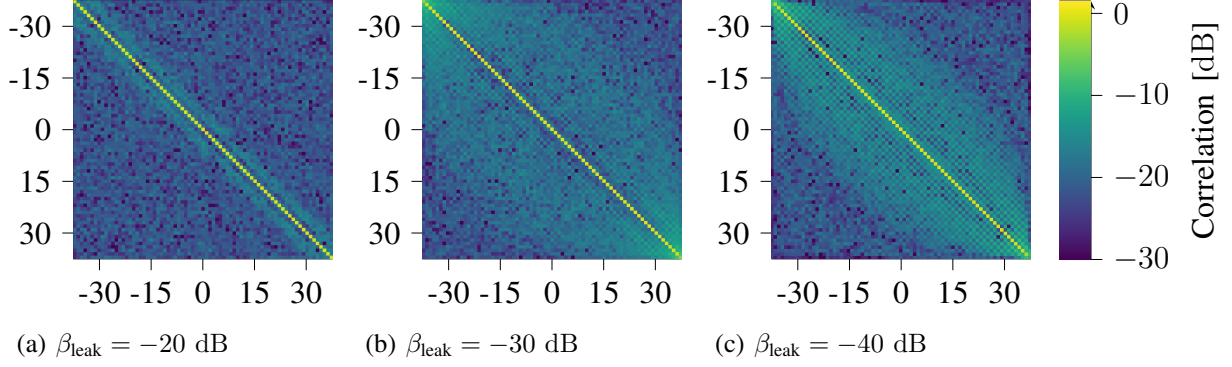


Fig. 9: Covariance matrices $\mathbb{E}_m [\mathbf{x}_m \mathbf{x}_m^H]$ for systems trained with different target ACLRs.

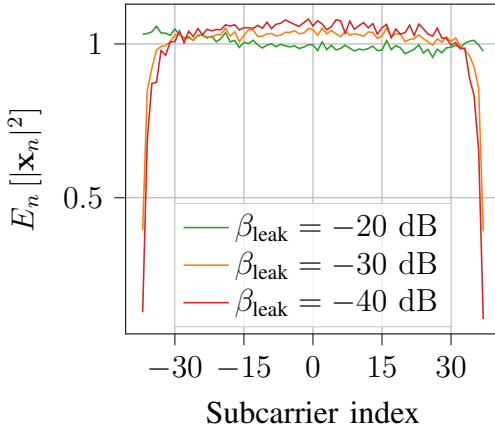


Fig. 10: Mean energy of the symbols transmitted on each subcarrier.

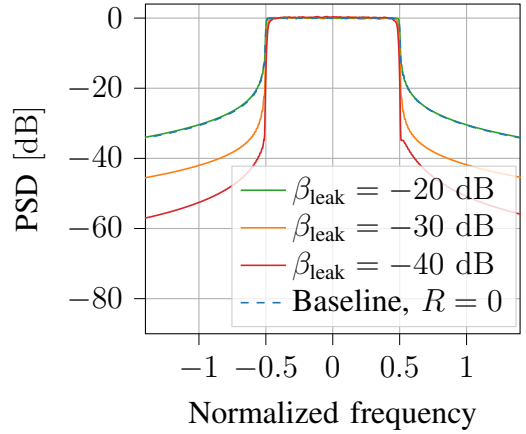


Fig. 11: PSD of four systems having no PAPR constraint.

trained with a lax ACLR constraint ($\beta_{\text{leak}} = -20$ dB) equally distributes the available energy on all subcarriers, which can be shown to maximize the information rate of the transmission. On the other hand, the systems trained with lower ACLR targets learn to reduce the energy of the subcarriers located at the RG edges, also contributing the out-of-band emissions reduction. The joint effect of the filtering and of the uneven energy distribution across subcarriers is visible in Fig. 11, where the power spectral densities (PSDs) of the compared systems are shown. One can see that the system trained with $\beta_{\text{leak}} = -20$ dB and the baseline have similar PSDs, while the PSDs of the systems trained with lower ACLR targets present significantly lower out-of-band emissions. It therefore appears that the improved ACLR allowed by the E2E system is the result of both reducing the power of the subcarriers located near the RG edges and the introduction of correlations between the transmitted symbols.

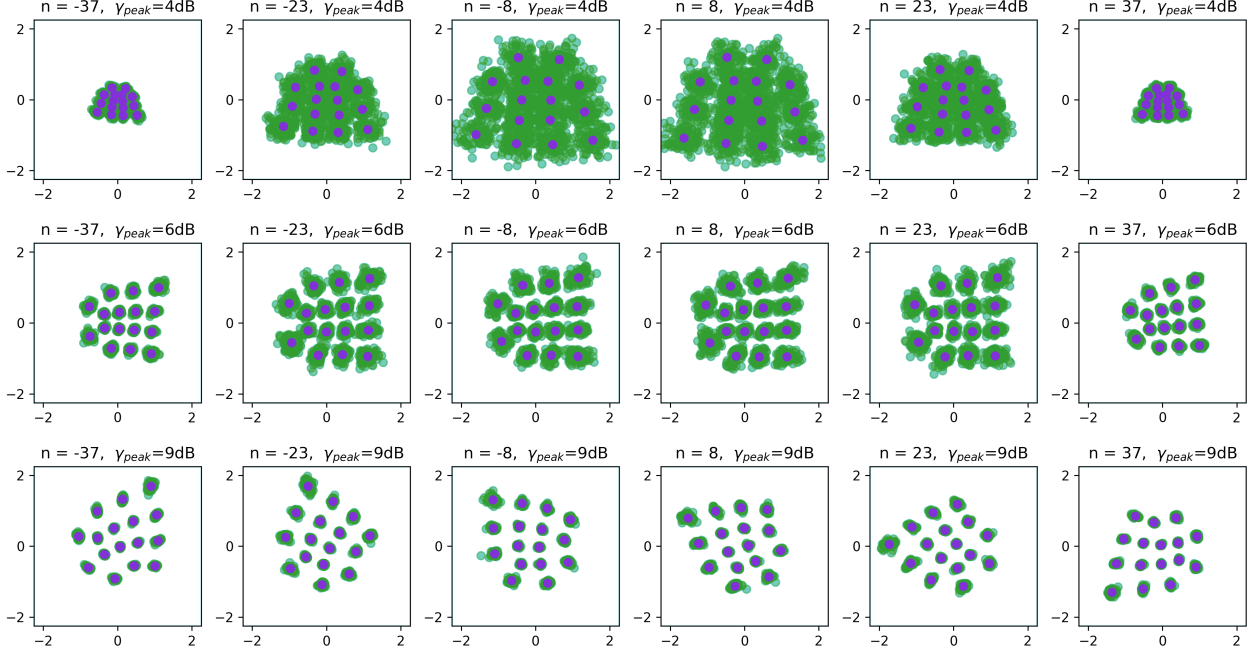


Fig. 12: Transmitted signals on six subcarriers for E2E systems trained with different PAPR targets but a lax ACLR constraint. The purple dots represent the center of each cluster.

2) *Interpreting the PAPR minimization process:* To understand how the neural transmitter and the optimization procedure enable significant PAPR reduction, it is insightful to look at the symbols transmitted for different PAPR targets, as illustrated in Fig. 12. The three rows represent E2E systems trained for PAPR targets of $\gamma_{\text{peak}} \in \{4, 6, 9\}$ dB, and the six columns show the signals transmitted on the subcarriers $n \in \{-37, -23, -8, 8, 23, 37\}$. All systems were trained with a lax ACLR constraint ($\beta_{\text{leak}} = -20$ dB). This figure was obtained by sending 25 RGs, and each green point represents one signal sent on the corresponding subcarrier. One can see that the signals are gathered into 2^K groups, that will be referred to as *clusters* in the following. It can be observed that for low PAPR targets ($\gamma_{\text{peak}} = 4$ dB), the clusters at the subcarriers located at the center of the RG exhibit more dispersion than the ones located near the RG edges. Moreover, the average energy of the transmitted signals also appears higher on the central subcarriers. On the contrary, for high PAPR targets ($\gamma_{\text{peak}} = 9$ dB), the clusters seem equally dispersed and the energy is evenly spread across the subcarriers. Finally, it can be noted that the positions of the clusters are not rotationally symmetrical, which should help the neural receiver in estimating and equalizing the channel.

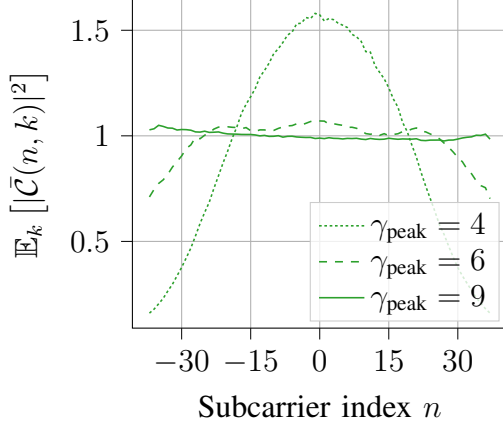


Fig. 13: Mean energy of the clusters centers per subcarrier.

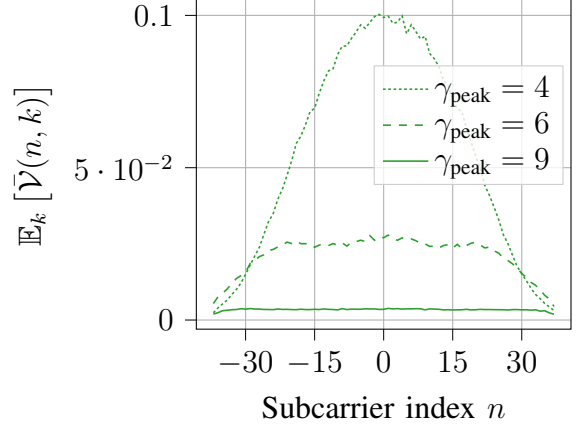


Fig. 14: Mean variance of the clusters per subcarrier.

To better understand the neural transmitter behavior, we index each cluster by a tuple (n, k) , where n is the subcarrier index and $k \in \{0, \dots, 2^K\}$ the index of the cluster for the n^{th} subcarrier. Let us denote by $\{\mathbf{b}^{(k)}\}_{1 \leq k \leq 2^K}$ the set of all possible vectors of bits indexed by their decimal representation, i.e., $\mathbf{b}^{(0)} = [0, 0]^T$, $\mathbf{b}^{(1)} = [0, 1]^T$, $\mathbf{b}^{(2)} = [1, 0]^T$, and $\mathbf{b}^{(3)} = [1, 1]^T$ for $K = 2$. We verified that each cluster corresponds to a unique vector of bits $\mathbf{b}^{(k)}$, and the center of these clusters are represented by purple dots in Fig. 12. For each E2E system, we define a new high-dimensional constellation $\bar{\mathcal{C}} \in \mathbb{C}^{N \times 2^K}$ that comprises the centers of the 2^K clusters on all N subcarriers. We denote by $\bar{\mathcal{C}}(n, k) = \mathbb{E}_{\mathbf{x}_m} [x_{m,n}^{(k)}]$ the k^{th} constellation point in the n^{th} subcarrier, where $x_{m,n}^{(k)}$ denotes the output of the neural transmitter for the RE (m, n) when $\mathbf{b}^{(k)}$ was given as input. Similarly, we define $\bar{\mathcal{V}} \in \mathbb{C}^{N \times 2^K}$, such that $\bar{\mathcal{V}}(n, k) = \mathbb{E}_{\mathbf{x}_m} [x_{m,n}^{(k)} x_{m,n}^{(k)*}]$ represents the variance of the cluster (n, k) .

Fig. 13 shows the mean energy of the constellation on each subcarrier for E2E systems trained with $\gamma_{\text{peak}} \in \{4, 6, 9\}$ dB and a lax ACLR constraint, corresponding to the three rows of Fig. 12. We can verify that when the PAPR constraint is lax ($\gamma_{\text{peak}} = 9$ dB), the energy is evenly distributed across the subcarriers. On the contrary, the border subcarriers are given less energy when a harsh constraint is applied ($\gamma_{\text{peak}} = 4$ dB). One explanation could be that the center subcarriers have longer wavelength, and therefore contribute less than their counterparts with shorter wavelengths. By focusing the available energy on these subcarriers, the neural transmitter jointly minimizes the probability of peaks in the analog waveform and decreases the number of FBSs that have a

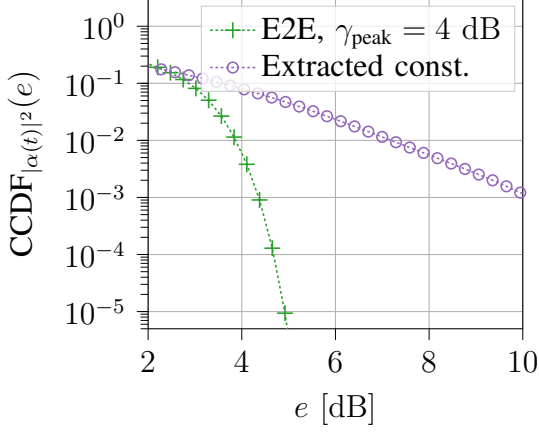


Fig. 15: CCDF of the power of the E2E system trained for $\gamma_{\text{peak}} = 4\text{dB}$ ($\beta_{\text{leak}} = -20\text{dB}$) and of a conventional system using its extracted constellation.

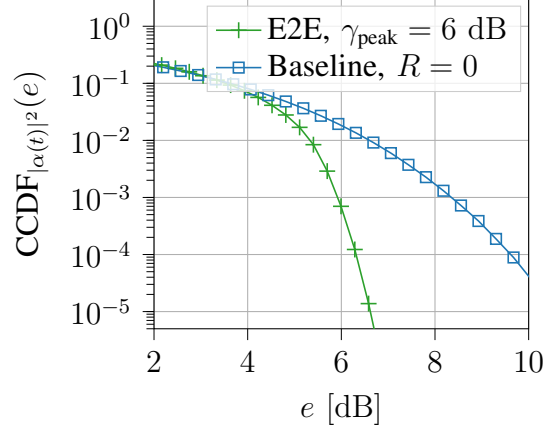


Fig. 16: CCDF of the power of the E2E system trained with $\gamma_{\text{peak}} = 6\text{dB}$ ($\beta_{\text{leak}} = -20\text{dB}$) and of the baseline using 16-QAM modulation and no PRT.

significant impact on them. Note that since the carrier frequency is typically much higher than the bandwidth of each subcarrier, the average power of the passband and baseband signals differs by a factor two but their maximum are approximately equal, which amounts to a roughly 3 dB difference between the passband and baseband PAPR [32]. Finally, the mean variance of the clusters on each subcarrier are plotted in Fig. 14 for the same three systems. One can observe that the clusters exhibit almost no variance with $\gamma_{\text{peak}} = 9\text{dB}$, but a high variance in the center frequencies with $\gamma_{\text{peak}} = 4\text{dB}$. These high variances observed with harsh PAPR constraints tend to indicate that the neural transmitter is able to slightly relocate the relevant FBSs in order to minimize the waveform PAPR. Overall, the transmitter seems to focus its energy on central subcarriers to reduce the probability of peaks and the number of relevant FBSs, and to adjust the positions of these FBSs to minimize the peak amplitudes.

In order to verify this claim, the complementary cumulative distribution function (CCDF) of the ratio between the instantaneous and average power of the transmitted signal is defined as

$$\text{CCDF}_{|\alpha(t)|^2}(e) = P(|\alpha(t)|^2 > e) \approx P\left(\left|\frac{z_{m,t}}{\mathbb{E}[z_{m,t}]}\right|^2 > e\right) \quad (36)$$

and is approximated by sending 10000 batches of 1000 RGs, each RG i being composed of $N = 75$ subcarriers and $M = 14$ OFDM symbols $\underline{z}_{m,t}^{[i]}$ oversampled with a factor 5. The CCDF

of two systems are presented in Fig. 15, the first one corresponds to the first row of Fig. 12, i.e., it is trained with the harshest PAPR constraint ($\gamma_{\text{peak}} = 9\text{dB}$) and a lax ACLR constraint ($\beta_{\text{leak}} = -20\text{dB}$). The second one is a conventional system that uses the constellation $\bar{\mathcal{C}}$ extracted from the aforementioned E2E system (and represented by purple dots in the first row of Fig. 12). The goal of this comparison is to evaluate the effect of the adjustment of the FBSs positions from the clusters centers operated by the transmitter. It can be seen that the CCDF of the E2E system is drastically lower than the one of the conventional system using the extracted constellation, indicating that the PAPR reduction is indeed performed through the FBSs position adjustments.

Finally, the CCDFs of the E2E system trained with $\gamma_{\text{peak}} = 6\text{dB}$ (and a lax ACLR constraint) and of a conventional QAM system are compared in Fig. 16. The E2E system corresponds to the second row of Fig. 12, and the two compared systems are respectively highlighted by a black circle and a black square in Fig. 7. One can see that the PAPR minimization process operated by the neural transmitter is particularly effective, as the CCDF of the E2E system is significantly lower despite the two systems enabling similar rates. Finally, it is also interesting to note that the CCDF of the system using the extracted constellation in Fig. 15 is higher than the one of the 16-QAM system in Fig. 16. This indicates that the underlying learned constellation alone has worse PAPR characteristics than a standard QAM, demonstrating the efficiency of the positional adjustments enabled by the neural transmitter.

V. CONCLUSION

In this paper, we proposed an end-to-end learning approach to design OFDM waveforms that meet specific constraints on the envelope and spectral characteristics. To that aim, the transmitter and receiver are modeled as two CNNs that perform high-dimensional modulation and demodulation, respectively. The training procedure first requires all optimization constraints to be expressed as differentiable functions that can be minimized through SGD. Then, a constrained optimization problem is formulated and solved using the augmented Lagrangian method. We evaluated the proposed approach on the learning of OFDM waveforms that maximize an information rate of the transmission while satisfying PAPR and ACLR constraints. Simulations were performed using 3GPP-compliant channel models, and results show that the optimization procedure is able to design waveforms that satisfy the PAPR and ACLR constraints. Moreover, the end-to-end system enables up to 30% higher throughput than a close to optimal implementation of a TR baseline with similar ACLR and PAPR. Evaluation insights revealed that the neural

transmitter achieves PAPR and ACLR reduction through a subcarrier-dependent filtering, an uneven energy distribution across subcarrier, and a positional readjustment of each constellation point. Future research directions include the training and evaluation of end-to-end systems with other optimization constraints and with larger RGs on channel model corresponding to medium- and high-mobility scenarios, possibly with hardware imperfections.

REFERENCES

- [1] H. Viswanathan and P. E. Mogensen, "Communications in the 6G Era," *IEEE Access*, vol. 8, pp. 57 063–57 074, 2020.
- [2] J. Hoydis, F. A. Aoudia, A. Valcarce, and H. Viswanathan, "Toward a 6G AI-Native Air Interface," *preprint arXiv:2012.08285*, 2021.
- [3] M. Goutay, F. A. Aoudia, J. Hoydis, and J.-M. Gorce, "End-to-End Learning of OFDM Waveforms with PAPR and ACLR Constraints," *preprint arXiv:2106.16039*, 2021.
- [4] Y.-C. Wang and Z.-Q. Luo, "Optimized Iterative Clipping and Filtering for PAPR Reduction of OFDM Signals," *IEEE Trans. Commun.*, vol. 59, no. 1, pp. 33–37, 2010.
- [5] B. S. Krongold and D. L. Jones, "PAR Reduction in OFDM via Active Constellation Extension," *IEEE Trans. Broadcast.*, vol. 49, no. 3, pp. 258–268, 2003.
- [6] B. Krongold and D. Jones, "An Active-Set Approach for OFDM PAR Reduction via Tone Reservation," *IEEE Trans. Signal Process.*, vol. 52, no. 2, pp. 495–509, 2004.
- [7] E. Nachmani, Y. Be'ery, and D. Burshtein, "Learning to Decode Linear Codes Using Deep Learning," in *Annu. Allerton Conf. on Commun., Control, and Comput.*, 2016, pp. 341–346.
- [8] D. Gündüz, P. de Kerret, N. D. Sidiropoulos, D. Gesbert, C. R. Murthy, and M. van der Schaar, "Machine Learning in the Air," *IEEE J. Sel. Areas Commun.*, vol. 37, no. 10, pp. 2184–2199, 2019.
- [9] M. Zhang, M. Liu, and Z. Zhong, "Neural Network Assisted Active Constellation Extension for PAPR Reduction of OFDM System," in *2019 11th Int. Conf. Wireless Commun. Signal Process. (WCSP)*, 2019, pp. 1–6.
- [10] B. Wang, Q. Si, and M. Jin, "A Novel Tone Reservation Scheme Based on Deep Learning for PAPR Reduction in OFDM Systems," *IEEE Commun. Lett.*, vol. 24, no. 6, pp. 1271–1274, 2020.
- [11] X. Wang, N. Jin, and J. Wei, "A Model-Driven DL Algorithm for PAPR Reduction in OFDM System," *IEEE Commun. Lett.*, 2021.
- [12] L. Li, C. Tellambura, and X. Tang, "Improved Tone Reservation Method Based on Deep Learning for PAPR Reduction in OFDM System," in *2019 11th Int. Conf. Wireless Commun. Signal Process. (WCSP)*, 2019.
- [13] M. Kim, W. Lee, and D.-H. Cho, "A Novel PAPR Reduction Scheme for OFDM System Based on Deep Learning," *IEEE Commun. Lett.*, vol. 22, no. 3, pp. 510–513, 2018.
- [14] C. Tellambura, "Computation of the continuous-time PAR of an OFDM signal with BPSK subcarriers," *IEEE Commun. Lett.*, vol. 5, no. 5, pp. 185–187, 2001.
- [15] F. Ait Aoudia and J. Hoydis, "End-to-end Learning for OFDM: From Neural Receivers to Pilotless Communication," *preprint arXiv:2009.05261*, 2020.
- [16] F. A. Aoudia and J. Hoydis, "End-to-end Waveform Learning Through Joint Optimization of Pulse and Constellation Shaping," *preprint arXiv:2106.15158*, 2021.
- [17] T. V. Luong, Y. Ko, M. Matthaiou, N. A. Vien, M.-T. Le, and V.-D. Ngo, "Deep Learning-Aided Multicarrier Systems," *IEEE Trans. Wireless Commun.*, vol. 20, no. 3, pp. 2109–2119, 2021.

- [18] B. Karanov, M. Chagnon, F. Thouin, T. A. Eriksson, H. Bülow, D. Lavery, P. Bayvel, and L. Schmalen, “End-to-End Deep Learning of Optical Fiber Communications,” *J. Lightw. Technol.*, vol. 36, no. 20, pp. 4843–4855, 2018.
- [19] S. Diamond and S. Boyd, “CVXPY: A Python-embedded modeling language for convex optimization,” *J. Mach. Learn. Research*, vol. 17, no. 83, pp. 1–5, 2016.
- [20] N. Andgart, “Peak and Power Reduction in Multicarrier Communication Systems,” Ph.D. dissertation, Lund University, 2005. [Online]. Available: <https://lup.lub.lu.se/search/ws/files/5589789/545619.pdf>
- [21] G. Böcherer, “Achievable rates for probabilistic shaping,” *arXiv preprint arXiv:1707.01134*, 2017.
- [22] D. P. Bertsekas, *Constrained Optimization and Lagrange Multiplier Methods*. Academic press, 2014.
- [23] J. Nocedal and S. Wright, *Numerical Optimization*. Springer Science & Business Media, 2006.
- [24] S. Cammerer, F. A. Aoudia, S. Dörner, M. Stark, J. Hoydis, and S. ten Brink, “Trainable Communication Systems: Concepts and Prototype,” *IEEE Trans. Commun.*, vol. 68, no. 9, pp. 5489–5503, 2020.
- [25] M. Honkala, D. Korpi, and J. M. J. Huttunen, “DeepRx: Fully Convolutional Deep Learning Receiver,” *preprint arXiv:2005.01494*, 2020.
- [26] D. Korpi, M. Honkala, J. M. J. Huttunen, and V. Starck, “DeepRx MIMO: Convolutional MIMO Detection with Learned Multiplicative Transformations,” *preprint arXiv:2010.16283*, 2020.
- [27] M. Goutay, F. A. Aoudia, J. Hoydis, and J.-M. Gorce, “Machine Learning for MU-MIMO Receive Processing in OFDM Systems,” *IEEE J. Sel. Areas Commun.*, vol. 39, no. 8, pp. 2318–2332, 2021.
- [28] K. He, X. Zhang, S. Ren, and J. Sun, “Identity Mappings in Deep Residual Networks,” in *Eur. Conf. Comput. vision*. Springer, 2016, pp. 630–645.
- [29] D.-A. Clevert, T. Unterthiner, and S. Hochreiter, “Fast and Accurate Deep Network Learning by Exponential Linear Units (ELUs),” *preprint arXiv:1511.07289*, 2016.
- [30] A. G. Howard, M. Zhu, B. Chen, D. Kalenichenko, W. Wang, T. Weyand, M. Andreetto, and H. Adam, “MobileNets: Efficient Convolutional Neural Networks for Mobile Vision Applications,” *preprint arXiv:1704.04861*, 2017.
- [31] S. Jaeckel, L. Raschkowski, K. Börner, and L. Thiele, “QuaDRiGa: A 3-D Multi-Cell Channel Model With Time Evolution for Enabling Virtual Field Trials,” *IEEE Trans. Antennas Propag.*, vol. 62, no. 6, 2014.
- [32] F. A. Eras, I. A. Carreño, T. Borja, D. J. Reinoso, L. Urquiza-Aguilar, and M. C. P. Paredes, “Analysis of the PAPR Behavior of the OFDM Passband Signal,” 2019.